ELSEVIER

Fluid Phase Equilibria 200 (2002) 93–110

FLUID PHASE EQUILIBRIA

www.elsevier.com/locate/fluid

Pressure-enthalpy driven molecular dynamics for thermodynamic property calculation II: applications

Loukas I. Kioupis, Gaurav Arya, Edward J. Maginn*

Department of Chemical Engineering, University of Notre Dame, Notre Dame, IN 46556, USA

Received 30 August 2001; accepted 28 November 2001

Abstract

The pressure-enthalpy driven molecular dynamics technique, developed in a companion paper [1], is used to compute various thermodynamic properties for the Lennard–Jones (LJ) fluid. These properties include the vapor–liquid coexistence curve, the critical point, the Joule–Thomson coefficient and inversion curve, and a complete vapor-compression refrigeration (VCR) cycle. The technique provides a simple and effective means of utilizing molecular dynamics to sample different thermodynamic state points. Results are as accurate as those obtained using Monte Carlo (MC) methods. © 2002 Elsevier Science B.V. All rights reserved.

Keywords: Molecular dynamics; Coexistence curve; Critical point; Joule–Thomson coefficient; Inversion curve; Thermodynamic cycle

1. Introduction

In a companion to the present paper [1], a molecular dynamics technique was presented that enables the direct simulation of isenthalpic pressure changes and isobaric enthalpy changes. The method, called pressure-enthalpy driven molecular dynamics (PHD-MD), was shown to provide an effective means for easily and rapidly changing the thermodynamic state point of a system within a molecular dynamics (MD) formalism. It was shown that reversible as well as irreversible thermodynamic cycles can be directly simulated. Two versions of the PHD-MD method were developed: a constraint-based method, referred to as $N\dot{P}\dot{H}_c$, and an extended system approach, referred to as $N\dot{P}\dot{H}_e$.

In the present work, we show how the PHD-MD technique can be utilized in a straightforward manner to calculate a range of different thermodynamic properties of practical interest, including the vapor–liquid coexistence curve and the Joule–Thomson coefficient and inversion curve. We also show how one can directly simulate a complete vapor-compression refrigeration (VCR) cycle as well as obtain accurate

* Corresponding author. Tel.: +1-574-631-5687; fax: +1-574-631-8366.
E-mail address: ed@nd.edu (E.J. Maginn).
URL: http://www.nd.edu/∼ed.

0378-3812/02/$ – see front matter
PII: S0378-3812(02)00015-8

estimates of critical points using the method. Thermodynamic calculations of this nature are most often performed using Monte Carlo (MC) methods, due to the ease with which different thermodynamic state points may be simulated with MC as compared to MD [1]. Unfortunately, there are a number of technical difficulties that must be overcome to incorporate efficient MC methods into generalized molecular modeling packages that use high-level forcefields. This is one of the barriers that has prevented the more widespread use of atomistic simulations for thermodynamic property calculations by industrial researchers and "non-experts" [2]. On the other hand, there are *many* commercial and academic codes that enable users to perform MD simulations on a wide range of molecules using advanced forcefields. The PHD-MD method can be easily incorporated into these existing MD codes, and thus enables thermodynamic calculations of the type described here to be readily performed with MD.

2. Simulation details

All calculations were performed on a Lennard–Jones (LJ) 12-6 fluid using either the $NP\dot{H}_c$ or $NP\dot{H}_e$ algorithm. Reduced units were used throughout. The simple LJ system was chosen because it has been extensively studied, making comparisions with other simulation techniques easier. We emphasize that the PHD-MD method is completely general, and can be applied to molecular as well as atomic systems. We have found that the $NP\dot{H}_e$ algorithm is preferred over the $NP\dot{H}_c$ method when working with a molecular system, as it avoids complications inherent in the application of constraints to internal degrees of freedom. We prefer the $NP\dot{H}_c$ method for atomic systems, although both methods yield identical thermodynamic results, as shown below and elsewhere [1]. Other details, including a full derivation of the equations of motion and definitions of variables referred to below, are provided in the companion paper to this work [1].

3. Applications

3.1. Joule–Thomson coefficient and inversion curve

The Joule–Thomson coefficient is a measure of how much the temperature of a fluid changes as pressure is changed at constant enthalpy and is defined as

$$\mu_{JT} \equiv \left(\frac{\partial T}{\partial P}\right)_H \tag{1}$$

It is an important property for fluids used in refrigeration and liquefaction processes [3]. It is also a critical parameter in the extraction of gas from high-pressure, high-temperature oil reservoirs [4]. Given its importance, it is desireable to *predict* μ_{JT} for a given fluid under various conditions. This can be done with equations of state, but unfortunately these equations are often inaccurate for multi-component mixtures at state points far from the experimental conditions at which the equation of state was parameterized. Thus, there is obvious utility in being able to *calculate* μ_{JT} directly from a molecular simulation of the fluid. This can be done in a straightforward fashion using the PHD-MD method by first driving the system to the desired intitial thermodynamic statepoint [1] and then recording the change in temperature that results from a small isenthalpic pressure change. Fig. 1 shows the results of many such calculations for a system comprised of 256 LJ particles at an enthalpy $H_{set} = 2.0$, using both the constraint ($NP\dot{H}_c$)

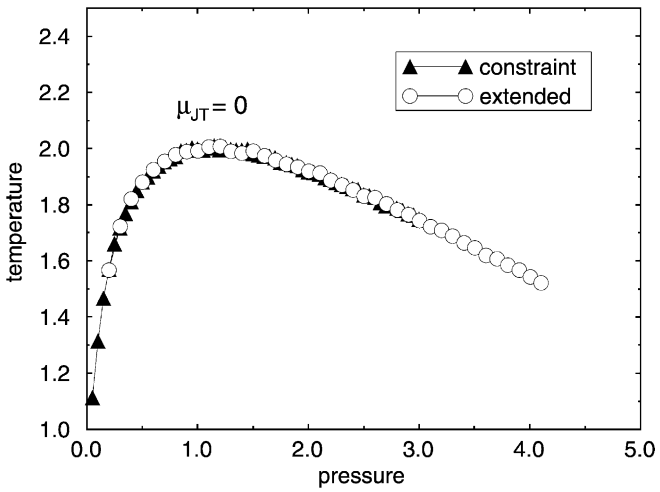

Fig. 1. Temperature vs. pressure at constant enthalpy $H = 2.0$. The slope of the curve is the Joule–Thomson coefficient. The solid symbols are results from the $N\dot{P}\dot{H}_c$ algorithm, while the open symbols are calculated using the $N\dot{P}\dot{H}_e$ method. They are identical within the statistical uncertainty of the calculations. The point at which $\mu_{JT} = 0$ is known as the inversion point.

and extended system ($N\dot{P}\dot{H}_e$) approach. For the $N\dot{P}\dot{H}_c$ method, a reduced time step of $\Delta t = 0.002$ was used, and the pressure was changed in small increments of $\Delta P = 0.05$ every 30,000 time steps. A Gear predictor–corrector algorithm was used to integrate the equations of motion. Each filled triangle in the figure represents one 30,000 time step calculation. Averages were computed over the last 25,000 steps after waiting 5000 steps for the system to equilibrate. For the results presented here, the pressure and enthalpy driver time constants were $R_P = 300$ and $R_H = 300$, respectively. Larger values (i.e. slower rates of change) were also tested at selected points and found to give identical results. For the $N\dot{P}\dot{H}_e$ results, shown as open circles in Fig. 1, a time step of $\Delta t = 0.0025$ was used, and each pressure interval was simulated for 15,000 time steps. The constants R_P and R_H were both set at 150 to obtain faster equilibration, and pressure increments were $\Delta P = 0.1$. A time-reversible reference system propagator algorithm (rRESPA) Verlet integrator was used for the simulations [5,6]. This integrator is more ammenable to the $N\dot{P}\dot{H}_e$ method than the $N\dot{P}\dot{H}_c$ method. Despite these small differences in simulation details, the isenthalps computed by the two methods agree perfectly. By examining Fig. 1 it can be observed that as the fluid is compressed, the temperature increases at low pressures but then decreases at high pressures. This means the Joule–Thomson coefficient is positive at low pressure, but negative at high pressure. The point where $\mu_{JT} = 0$ is known as an *inversion point*. For the enthalpy chosen here ($H_{set} = 2.0$), the inversion point occurs at $P = 1.15$ and $T = 2.0$.

The molecular-level basis for the inversion point, although well understood, is made obvious in Fig. 2 by noting how various thermodynamic quantities change under isenthalpic compression. The potential energy, Φ, decreases as the pressure increases. This is due to the fact that attractive intermolecular interactions increase as the molar volume V (i.e. intermolecular separation) decreases. The change is greatest at low pressure, where molar volume changes are greatest. This can be seen clearly in Fig. 3, which shows that the compression ratio is greatest at low pressure. At higher pressure there has already been a significant reduction in molar volume; increasing the pressure does little to change the relative separation of molecules. This of course is due to the nature of the LJ potential function, which has a

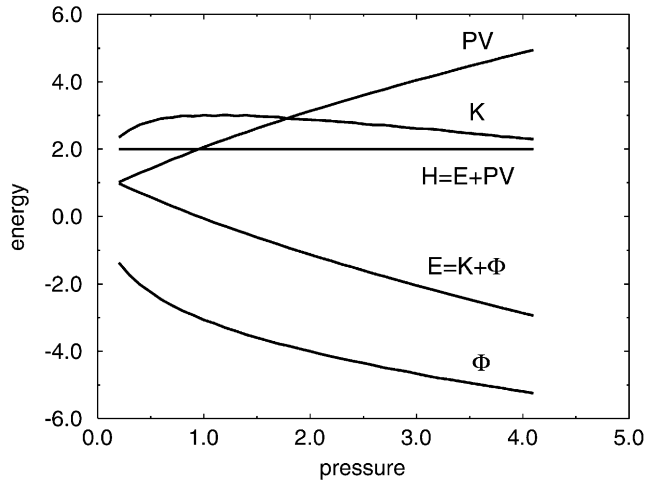

Fig. 2. The dependence of the different energy terms on pressure for the isenthalp $H = 2.0$. Pressure is P, kinetic energy is K and potential energy is Φ. Other symbols are defined in the text or figure.

steep repulsive core at small intermolecular separation. Since the PV energy in Fig. 2 increases at nearly a constant rate with pressure, the kinetic energy K has to go through an inversion point to compensate for the changes in PV and Φ while still keeping H constant.

The locus of pressure–temperature points where $\mu_{JT} = 0$ is known as the Joule–Thomson inversion curve. Inversion curves are important for the same reason Joule–Thomson coefficients are important. They are extremely difficult to obtain experimentally, since it is necessary to measure volummetric properties at up to five times the critical temperature and 12 times the critical pressure [7]. The prediction of inversion curves is among the severest tests of an equation of state, or for that matter, of a molecular

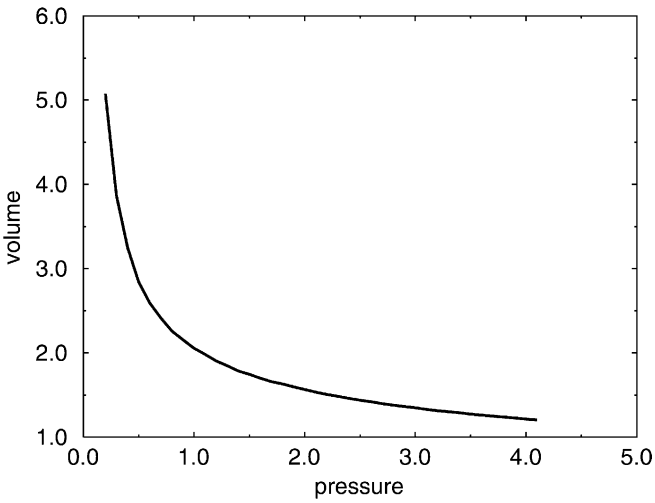

Fig. 3. Molar volume vs. pressure at $H = 2.0$.

Table 1
Joule–Thomson inversion temperature T and pressure P at different molar enthalpies h using the constraint and extended system methods. The results shown are in reduced units. Numbers in the parentheses represent statistical uncertainties in the last reported digits

h	Constraint		Extended system	
	P	T	P	T
−1.5	0.47(2)	1.30(1)	0.45(2)	1.30(1)
−0.5	0.67(2)	1.49(1)	0.70(3)	1.48(1)
0.0	0.83(3)	1.59(2)	0.84(2)	1.58(2)
0.5	0.88(3)	1.68(2)	0.94(3)	1.68(2)
2.0	1.15(3)	2.00(2)	1.15(3)	2.00(2)
3.0	1.25(4)	2.23(2)	1.24(4)	2.23(2)
4.0	1.29(6)	2.47(2)	1.32(7)	2.47(2)
5.0	1.32(4)	2.73(3)	1.35(4)	2.73(3)
6.0	1.40(4)	3.00(3)	1.40(4)	3.00(3)
7.0	1.36(4)	3.28(3)	1.32(4)	3.28(3)
9.0	1.20(4)	3.89(4)	1.20(4)	3.88(4)
11.0	1.01(3)	4.55(4)	1.00(3)	4.54(4)
12.0	0.85(3)	4.90(5)	0.85(4)	4.89(5)
13.0	0.72(4)	5.26(5)	0.70(3)	5.25(5)
15.0	0.30(3)	6.00(6)		

simulation method or intermolecular forcefield. The inversion curve for the LJ fluid was computed using the PHD-MD method in the following way. Several isenthalps were simulated in a manner similar to that used to generate the isenthalp shown in Fig. 1. Each was fit with a polynomial, and the inversion point was then determined analytically and confirmed graphically. The results of these computations, using both the contraint and extended system methods, are presented in Table 1 and are plotted in Fig. 4 as open squares and open triangles, respectively. The two methods yield identical inversion curves, within the statistical accuracy of the simulations. The inversion curve predicted by the LJ equation of state developed by Johnson and et al. [8] is shown as a solid line, while previous simulation results from Colina and Müller [9,10], Heyes and Llaguno [11], and Escobedo and Chen [12] are also shown. Since the equation of state was developed using several different simulation results and is highly accurate for many other properties, it is safe to assume that it is the "correct" result.

Each of the simulation results shown in Fig. 4 were obtained in a different manner. Heyes and Llaguno [11] were the first to attempt the calculation of the LJ inversion curve using molecular simulation. These authors attempted to generate isenthalps using standard isothermal–isobaric (*NPT*) MD simulations. They adjusted the temperature of the simulations using a least square extrapolation procedure to obtain predetermined values of the enthalpy. Their method yields reliable values only at low temperature; at temperatures >2.0, the method shows a great deal of scatter and does not conform with the other results. Colina and Müller [9,10] used *NPT* Monte Carlo simulations to generate a series of isobars. They estimated the inversion point by looking for the location of an extrema in the isobars, much like the way in which inversion points are obtained experimentally. Their results follow the prediction from the equation of state much more faithfully than do those of Heyes and Llaguno, although there is some discrepancy at higher temperatures. Escobedo and Chen have recently reported results for the LJ inversion curve using a novel

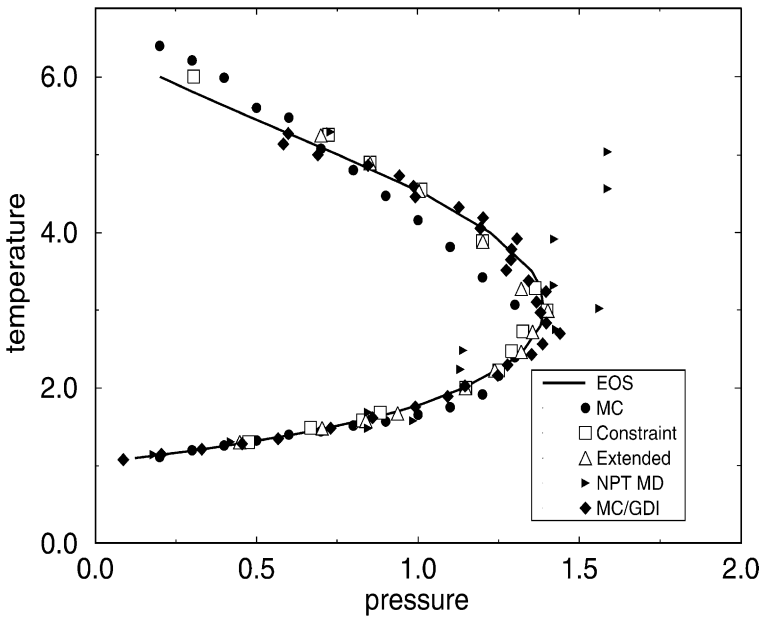

Fig. 4. Inversion curve for the LJ fluid. Open squares are simulation results from the constraint method, while open triangles are from the extended system method simulations. Filled circles are from the Monte Carlo simulations of Colina and Müller [9,10]. Filled triangles are from MD simulations by Heyes and Llaguno [11], and filled diamonds are MC/Gibbs–Duhem integration results from Escobedo and Chen [12]. The solid line is the prediction from an accurate equation of state [8].

integration scheme in conjunction with *NPT* Monte Carlo simulations [12]. Their results follow those of Colina and Müller, but show an even closer match with the equation of state prediction. The fact that the MC simulation results are more accurate than the results obtained using conventional MD comes as no surprise. As stated in a previous work [1], MC methods are generally superior to MD for thermodynamic property calculation, mainly because one can exert much greater control over the state points being simulated. The results in Fig. 4 confirm, however, that the PHD-MD method does not suffer from the same drawbacks as does conventional MD. The PHD-MD results match the equation of state prediction and the simulation results of Escobedo and Chen almost exactly. In particular, the high temperature leg of the inversion curve, where experimental and simulation uncertainty is greatest, is accurately captured by the simulations. This stringent test demonstrates that the PHD-MD technique enables one to easily move between state points to accurately compute thermodynamic properties while still utilizing a relatively straightforward MD technique.

3.2. Vapor-compression refrigeration cycle

The PHD-MD method can be used to calculate a number of other properties of practical interest. In this section, the technique is used to simulate a complete VCR cycle for the LJ fluid. The VCR cycle simulated here is shown schematically in Fig. 5. We stress that this is not a particularly realistic nor optimal refrigeration cycle. An actual VCR cycle would operate well below the critical pressure. This particular cycle was chosen for convenience and to demonstrate the capabilities of the PHD-MD method.

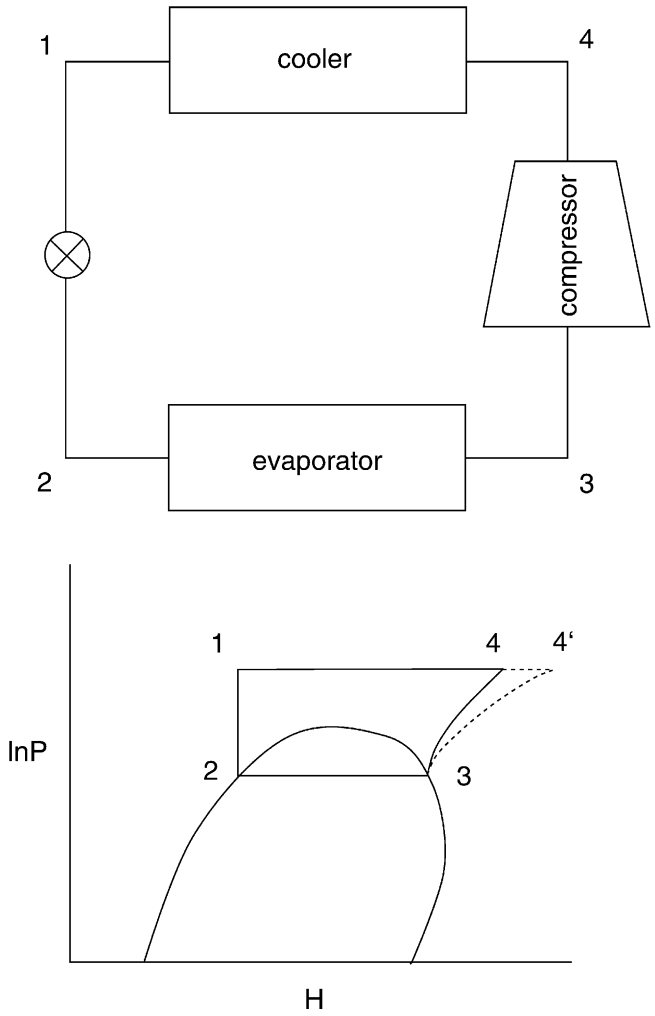

Fig. 5. A schematic and P–H plot of the vapor-compression refrigeration cycle simulated in this work.

The fluid goes through different regions of the LJ fluid phase diagram, including the supercritical, liquid, vapor, and two phase vapor–liquid region. It thus provides an interesting system of study, as well as a rigorous test of the method.

VCR is the method most commonly employed in residential and automotive cooling applications. The VCR cycle involves the following four steps [3]:

1. Starting from state 1, the fluid (i.e. refrigerant) passes through an adiabatic valve where it undergoes a Joule–Thomson expansion (path 1→2). The pressure of the fluid is reduced to the saturation liquid pressure at state 2.
2. Next, the refrigerant goes through an evaporator that operates under constant pressure conditions (path $2 \rightarrow 3$). During this stage heat is absorbed by the refrigerant, which results in an increase in enthalpy ΔH_{23}. The refrigerant is evaporated, reaching a saturated vapor state (state 3). The amount of heat

ΔH_{23} is the amount of heat that is removed from the chamber being refrigerated and determines the cooling action of the refrigerant.

3. During the path $3 \rightarrow 4$, the vapor exiting the evaporator is compressed back to the initial pressure, which is the operational pressure of the cooler. This is done using a compressor that typically operates under adiabatic conditions. Work is done on the fluid during this process, so the enthalpy of the fluid increases. For an ideal compressor this process takes place isentropically and the increase in the enthalpy of the fluid equals to $\Delta H_{34} = \int V \, \mathrm{d}P$. In fact, no real compressor performs a true isentropic compression. Usually, this step is irreversible due to friction between the machine elements and the fluid. Since the compressor operates under adiabatic conditions, the irreversible entropy production results in an additional increase in enthalpy over that which results from an isentropic process. Therefore, a typical route during this stage is shown in Fig. 5 with the dashed line.
4. Finally, in path $4 \rightarrow 1$, the refrigerant flows through a heat exchanger (i.e. a cooler). Heat is removed under isobaric conditions and the fluid is brought back to its initial state 1. In an actual VCR cycle, the heat exchanger is typically a condenser, but is represented simply as a cooler for this example.

The refrigeration cycle shown in Fig. 5 can be *directly* simulated using the PHD-MD method. To demonstrate this, we consider the refrigerant to be a LJ fluid consisting of 500 particles. The $NP\dot{H}_c$ method is used along with a predictor–corrector integration scheme and a reduced time step of $\tau = 0.001$. To generate reversible paths, very small changes in state variables are made, similar to that described in the previous paper [1]. Small step changes in pressure or enthalpy are imposed every 60,000 time steps and equilibrium averages are computed over the last 50,000 time steps of each interval. A series of equilibrium points are generated with this process and the paths produced are shown in Fig. 6.

To simulate the cycle shown in Fig. 6, four independent state variables that define the operational conditions of the VCR cycle must be specified. For the calculations performed here, we chose the operational pressures of the cooler $P_c = 0.3$ and evaporator $P_e = 0.0772$. Saturated liquid and vapor enthalpies

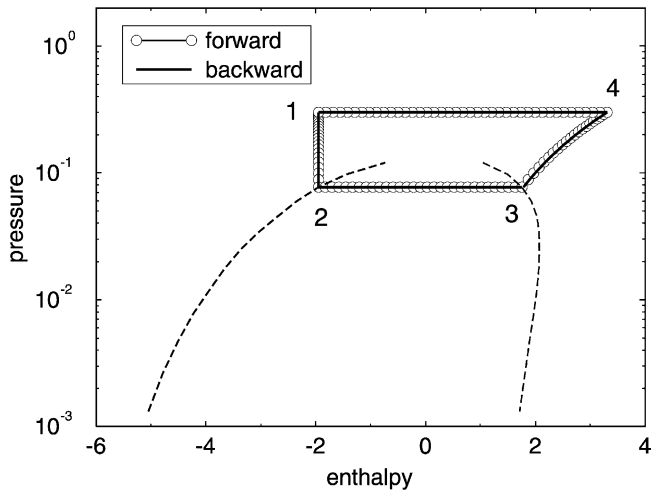

Fig. 6. The P–H plot of the simulated vapor-compression refrigeration cycle. Open symbols show the simulation results for a "forward" cycle (points $1 \rightarrow 2 \rightarrow 3 \rightarrow 4$), while the solid line shows a simulation of the "reverse" cycle ($1 \rightarrow 4 \rightarrow 3 \rightarrow 2$). The paths are identical, indicating that the simulations generate reversible cycles.

Table 2
Average equilibrium quantities for the forward ($1 \rightarrow 2 \rightarrow 3 \rightarrow 4 \rightarrow 1$) and backward ($1 \rightarrow 4 \rightarrow 3 \rightarrow 2 \rightarrow 1$) cycles. The results shown are in reduced units. Numbers in the parentheses represent statistical uncertainties in the last reported digits

State point	P	h	e	T	v
Forward					
1	0.300(0)	−1.948(0)	−2.427(4)	1.223(7)	1.598(7)
2	0.0772(0)	−1.948(0)	−2.084(3)	1.206(6)	1.759(5)
3	0.0772(0)	1.757(0)	0.986(6)	1.195(4)	10.0(1)
4	0.300(0)	3.306(2)	1.711(9)	1.959(5)	5.32(3)
1	0.300(0)	−1.948(0)	−2.426(4)	1.226(6)	1.595(5)
Backward					
1	0.300(0)	−1.948(0)	−2.425(3)	1.232(8)	1.591(5)
2	0.0772(0)	−1.948(0)	−2.084(3)	1.199(6)	1.764(5)
3	0.0772(0)	1.784(3)	0.995(6)	1.194(4)	10.22(9)
4	0.300(0)	3.306(1)	1.709(5)	1.958(5)	5.32(2)
1	0.300(0)	−1.948(0)	−2.426(4)	1.227(8)	1.595(5)

($H_2 = -1.948$ and $H_3 = 1.757$) were chosen by referring to previous simulation work of Lotfi et al. [13], where they report phase equilibria data for the LJ fluid obtained using the $NPT +$ test particle method. The cycle was simulated using the following process:

- *Path* $1 \rightarrow 2$: starting from the state point of $P_{\text{set}} = 0.3$ and $H_{\text{set}} = -1.948$, which represents the high-pressure low-enthalpy state (state 1) at the exit of the cooler (see Fig. 6), an isenthalpic expansion is performed by changing P_{set} from 0.3 to the saturation pressure 0.0772 (state 2). During this procedure a series of 20 equilibrium points were generated that represent the true isenthalpic path $1 \rightarrow 2$ (see Fig. 6). The average quantities computed at the initial (state 1) and final (state 2) equilibrium points are shown in Table 2.
- *Path* $2 \rightarrow 3$: starting from state 2, the evaporation stage (path $2 \rightarrow 3$) is generated by increasing H_{set} gradually from $H_2 = -1.948$ to $H_3 = 1.757$. During this process 30 step changes were imposed. The final state conditions (state 3) are presented in Table 2.
- *Path* $3 \rightarrow 4$: in the path $3 \rightarrow 4$, the fluid undergoes an isentropic compression. To see how this is accomplished, we refer to our previous work [1], where it was shown that the time rate of change in the enthalpy under the $N\dot{P}\dot{H}_{\text{c}}$ algorithm is

$$\dot{H} = \dot{P}V - \alpha \sum_i m_i v_i^2 \tag{2}$$

where $\dot{P}$ is the time rate of change in pressure, the sum is over all atoms i of mass m_i and velocity v_i. The coefficient α constrains the enthalpy and is related to the change in entropy of the system via the following equation

$$-\alpha \sum_i m_i v_i^2 = T\dot{S} \tag{3}$$

An isentropic compression can, thus, be accomplished by removing the enthalpy driver and setting $\alpha = 0$, as in the standard *NPH* constraint algorithm. Unlike the standard method, however, the differential

pressure driver $\dot{P}$ remains to drive the pressure from states 3 to 4. Since $\alpha = 0$, the entropy is constant, but the enthalpy changes according to the first law of thermodynamics for adiabatic compressibility, $\Delta H = \int V \, \mathrm{d}P$. During this process 20 equilibrium points were generated. The pressure was increased to 0.3 and the path followed is shown in Fig. 6. The final value of the enthalpy, along with other thermodynamic equilibrium average quantities are shown in Table 2.

- *Path* $4 \rightarrow 1$: finally, the isobaric cooling process ($4 \rightarrow 1$) was simulated. The same approach as that used in stage $2 \rightarrow 3$ was utilized. Starting from the final value of the enthalpy generated during the compression stage (state 4), small reductions in H_{set} were performed in 40 steps until the system was driven to its initial enthalpy at state 1 ($H_1 = -1.948$). Comparing the initial and final states (states 1) from Table 2, we see that the cycle closes and the system returns to its initial state correctly.

The refrigeration cycle was also simulated backwards (i.e. following the route $1 \rightarrow 4 \rightarrow 3 \rightarrow 2 \rightarrow 1$). The forward and backward paths are shown in Fig. 6 as open symbols and a solid line, respectively. A P–V plot of the cycle is also shown in Fig. 7. The agreement between the two routes is excellent, with both cycles returning the system to its initial state 1. Results of the simulations at the final states after each backward path are also presented in Table 2. The results of the saturated temperature and saturated volumes (states 2 and 3) computed during the forward and backward cycles compare very well with the values of $T = 1.2$, $v^{\mathrm{l}} = 1.766$ and $v^{\mathrm{v}} = 10.13$ reported by Lotfi et al. [13] (see Table 2).

The energy balances are calculated during the cycle using the first law of thermodynamics, with results presented in Table 3. The calculations were performed for both the forward and backward cycles. The molar energy terms shown in Table 3 are not time integrals over the course of the entire simulation, but rather were calculated from the averages at the equilibrium states (1, 2, 3, or 4) of the cycle. The enthalpy Δh and internal energy Δe differences reported in Table 3 were computed using the final and initial states in each path. The work terms $\int v \, \mathrm{d}P$ and $\int P \, \mathrm{d}v$ were calculated by integrating the routes shown in Fig. 7, and the quantities $\int T \, \mathrm{d}s$ were calculated from the differences $\int T \, \mathrm{d}s = \Delta h - \int v \, \mathrm{d}P$ and $\int T \, \mathrm{d}s = \Delta e + \int P \, \mathrm{d}v$. Examining the results presented in Table 3, we see that $\Delta h = 0$ and $\Delta e = 0$ since the simulations produce a closed cycle. The quantity $\int T \, \mathrm{d}s$ computed from the time integral $-\int 3kT\alpha \, \mathrm{d}t$

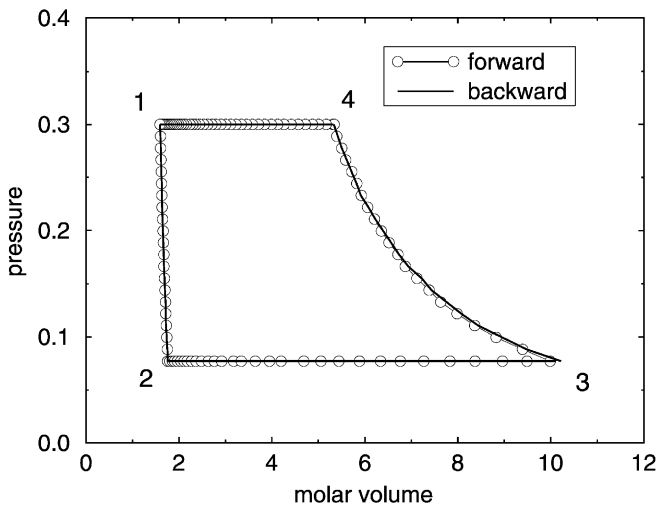

Fig. 7. Simulated vapor-compression cycle on a P–V plot.

Table 3
Energy balance calculations for the forward ($1 \rightarrow 2 \rightarrow 3 \rightarrow 4 \rightarrow 1$) and backward ($1 \rightarrow 4 \rightarrow 3 \rightarrow 2 \rightarrow 1$) cycles. The results shown are in reduced units. Numbers in the parentheses represent statistical uncertainties in the last reported digits

Path	Δh	$\int v\,\mathrm{d}P$	$\Delta h - \int v\,\mathrm{d}P$	Δe	$\int P\,\mathrm{d}v$	$\Delta e + \int P\,\mathrm{d}v$	$-\int 3kT\alpha\,\mathrm{d}t$
Forward							
$1 \rightarrow 2$	0.000(0)	−0.372(2)	0.372(2)	0.343(7)	0.028(2)	0.371(9)	0.368(8)
$2 \rightarrow 3$	3.705(0)	0.000(1)	3.705(1)	3.070(9)	0.635(2)	3.705(11)	3.688(30)
$3 \rightarrow 4$	1.549(2)	1.527(2)	0.022(4)	0.725(15)	−0.702(2)	0.023(17)	–
$4 \rightarrow 1$	−5.254(2)	0.000(1)	−5.254(3)	−4.137(13)	−1.117(3)	−5.254(16)	−5.288(42)
Sum	0.000(1)	1.155(6)	−1.155(8)	0.001(8)	−1.156(9)	−1.155(17)	−1.232(80)
Backward							
$2 \rightarrow 1$	0.000(1)	0.372(2)	−0.372(3)	−0.341(6)	−0.031(2)	−0.372(8)	−0.376(8)
$3 \rightarrow 2$	−3.732(4)	0.000(1)	−3.732(5)	−3.079(9)	−0.653(1)	−3.732(10)	−3.742(31)
$4 \rightarrow 3$	−1.522(4)	−1.538(2)	0.016(6)	−0.714(11)	0.727(2)	0.013(13)	–
$1 \rightarrow 4$	5.254(1)	0.000(1)	5.254(2)	4.135(9)	1.118(2)	5.253(11)	5.230(42)
Sum	0.000(1)	−1.166(6)	1.166(7)	0.001(8)	1.161(7)	1.162(15)	1.112(81)

during the course of the simulation is also shown for comparison. The results agree despite the numerical errors, noise and irreversibilities inherent in a continuous run.

As indicated in our previous work [1], it is possible to introduce irreversibilities by using a very fast compression rate. It is for this reason that values of the pressure change rate constants (k_P) and pressure step sizes (ΔP_{set}) were chosen carefully so as to obtain an isentropic compression in moving between states 3 and 4. It is also possible to generate irreversibilities in the compression path ($3 \rightarrow 4$) by using too large a timestep. Fig. 8 shows results for the compression path ($3 \rightarrow 4$) from simulations using a

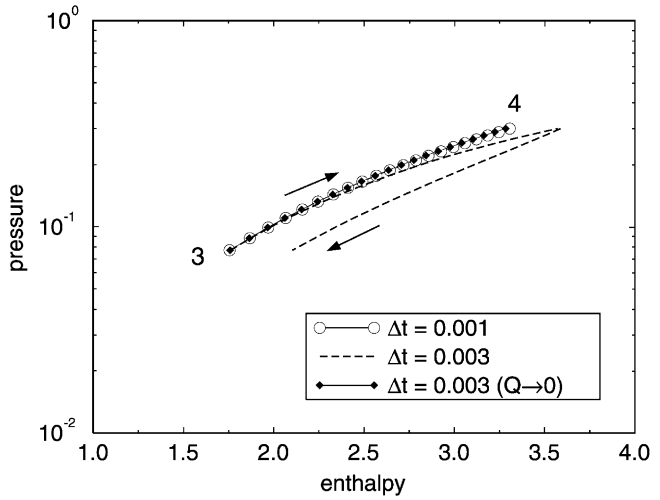

Fig. 8. P–H paths taken during compression–decompression steps ($3 \leftrightarrow 4$) using different simulation timesteps. Open circles are for a reversible path with a small timestep. The dashed line shows the irreversibilities introduced by using too large a timestep. The solid diamonds show that a reversible path may be recovered even using a large timestep by constraining the entropy of the system during compression.

small timestep ($\tau = 0.001$) and a larger time step of $\tau = 0.003$. As mentioned previously, in generating the path between states 3 and 4, the PHD-MD method reduces to an *NPH* MD simulation in which the pressure is being driven (i.e. the enthalpy controller $\alpha = 0$). Clearly, the forward and reverse paths do not coincide when the large timestep is used, indicating that the simulation is not reversible. The origin of the irreversibility is the accumulation of numerical error that effectively causes an increase in the entropy of the system. This drift is highly dependent on the size of the time step. Ideally, one would like to use as large a timestep as possible but still simulate reversible paths. This is especially important when simulating large molecules whose equilibration times are much longer than that of LJ atoms. For these systems, the use of large timesteps is essential to prevent simulations from requiring prohibitive computer resources.

This problem can be remedied by resorting to the same concepts as were used to drive pressure and enthalpy in the PHD-MD method. To guarantee that an isentropic route is *always* obtained, a new friction coefficient α_S is reintroduced into the equations of motion in place of α and the term $Q = \int \mathrm{d}H - \int V\,\mathrm{d}P$ is forced to zero (see [1] for details). The friction coefficient α_S serves to *contrain the entropy* during the simulation. Starting from

$$\dot{H} - V\dot{P} = \dot{Q} \tag{4}$$

and substituting Eq. (2) for $\dot{H}$ leads to

$$\alpha_S = -\frac{\dot{Q}}{\sum_i m_i v_i^2} \tag{5}$$

A differential controller is used to drive the term $\dot{Q}$ to zero ($\dot{Q} \to 0$).

$$\dot{Q} = k_Q(-Q) = -k_Q\left(\int \mathrm{d}H - \int V\,\mathrm{d}P\right) \tag{6}$$

Substituting the above driver into Eq. (5) results in a new set of equations of motion (refer to [1] for implementation details). In order to use this "entropy control" scheme, the integrals $\int \mathrm{d}H$ and $\int V\,\mathrm{d}P$ need to be continuously computed during the course of the simulation. We use a simple numerical Simpson method, although any suitable technique will do. The new equations of motion automatically transfer heat to or from the system so that the enthalpy increase $\int \mathrm{d}H$ is always equal to the work $\int V\,\mathrm{d}P$ imposed by the compression, thereby generating a true isentropic path. The simulated system is no longer adiabatic ($\alpha \neq 0$). Indeed, some heat is removed from the system in order to "dissipate" the entropy generated by numerical drifts. This entropy control scheme can be thought of as using an equivalent Newton–Raphson technique to rescale everything in order to achieve isentropic path generation, although it achieves this in a smooth and natural manner.

The solid diamonds in Fig. 8 show the results of a compression–decompression cycle between states 3 and 4 using the entropy control scheme and a large time step $\tau = 0.003$. The paths are now reversible and indistinguishable from those generated using a time step $\tau = 0.001$. In fact, we simulated the entire VCR cycle with a larger time step of $\tau = 0.003$ and found excellent agreement with the simulations performed using the smaller $\tau = 0.001$ time step. The imposition of the various drivers stabilizes the system so that larger time steps can be used. In this way, the PHD-MD technique has similarities with other techniques that use damping methods to utilize larger timesteps [14].

From a practical standpoint, one is most interested in understanding how a particular fluid or fluid mixture performs as a refrigerant. That is, one would like to know what the operating temperatures and

pressures are of the evaporator and cooler (condenser), as well as how much heat can be carried by a given quantity of fluid. All these design parameters can be determined for a given refrigerant from PHD-MD simulations without resorting to the detailed cycle calculations performed here. One simply must drive the system to each of the four state points shown in Fig. 5 and calculate equilibrium properties at each of these conditions. For this purpose, there is no need to impose small step changes and generate the full paths, as was done here. Therefore, the operational conditions of the cycle can be determined quickly for any fluid for which accurate potential parameters exist. It is not necessary to know in advance what the thermodynamic state point is at each point in the VCR cycle. As has been shown here, only the operational pressures (P_c and P_e) and saturation enthalpies are required. As an alternative to choosing the saturation enthalpies (which may not be known), the heat or work change for a given leg of the cycle could be specified and used to locate the next point in the cycle. In any case, only four independent variables are required to perform the VCR cycle calculation. In essence, the PHD-MD method enables one to perform VCR cycle calculations in much the same way that would be done with knowledge of the experimental *PH* phase diagram for the refrigerant. In this case, however, the phase diagram does not need to be known a priori, only the intermolecular potential function is required. The simulation serves as a substitute for the phase diagram. Thus, the PHD-MD method provides a straightforward approach to "translating" the potential function into a functional *PH* diagram. This method should be useful in the search for safe and environmentally benign refrigerants.

Finally, we show in Fig. 9 a T–V plot of the VCR cycle. Interestingly, the temperature during the evaporation stage is not constant at its saturation value, but instead shows an oscillation. This oscillation is similar to pressure oscillations seen in the LJ coexistence region during canonical ensemble MC simulations [15,16]. These oscillations are attributed to the free energy costs associated with creating vapor–liquid interfaces in the finite-sized system. Since in the PHD-MD simulations the pressure (and enthalpy) are constrained and thus cannot vary, the temperature shows the fluctuation. The temperature behavior within this metastable region is also reminiscent of the pressure fluctuations observed when

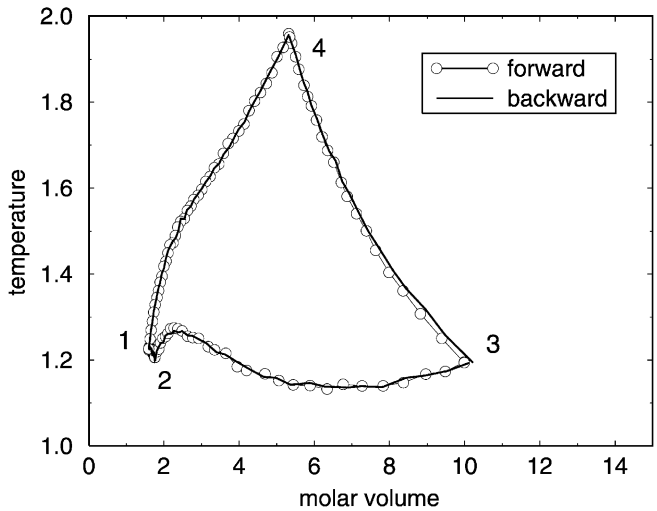

Fig. 9. The temperature–volume trace that results from the forward and backward simulation of the vapor-compression refrigeration cycle. Note the change in temparature that occurs during the phase change between points 2 and 3.

an isotherm for a cubic equation of state is plotted (so-called "van der Waals loops"). In the two phase unstable region, a cubic equation of state predicts a pressure that goes through a minimum at small molar volume and a maximum at large molar volume. In Fig. 9, the temperature goes first through a maximum and then a minimum as the enthalpy (molar volume) increases. As described in the next section, this information can be exploited to determine vapor liquid coexistence curves and estimate critical points using MD.

3.3. The two phase region

Arguably, one of the most important practical applications of molecular simulation is the determination of phase coexistence. Among the many methods used to compute phase behavior, three have emerged as the most popular: the Gibbs ensemble MC procedure [17,18], the Gibbs–Duhem integration method [19], and histogram reweighting grand canonical MC schemes [20,21]. Although the Gibbs–Duhem method can be used in conjunction with isothermal–isobaric MD, it is typically carried out using MC simulations. The other two simulation methods are strictly MC techniques. The Gibbs–Duhem method has an advantage over the other two methods in that it does not require particle exchanges or insertions. These insertion moves can be quite difficult to perform for dense phases. Although the Gibbs–Duhem method does not suffer from this limitation, it does require an initial point on the saturation curve [19], which must come from some other source.

The PHD-MD method can be used to compute coexistence curves. To do this, the enthalpy of the system is slowly changed at constant pressure. Isobars at pressures above the critical point will show a monotonic increase in the density as the enthalpy is reduced. Isobars below the critical point will pass through the two phase region. As was seen in Fig. 9, the temperature will oscillate due to the formation of vapor–liquid interfaces. At the critical pressure, the isobar should exhibit an inflection point. The coexistence envelope can be estimated using a procedure analogous to a standard Maxwell construction, although in the present case the simulation is along an isobar rather than an isotherm. To show how this is done, we start with the equifugacity condition between the pure liquid and vapor phase [22]

$$\ln \phi^{\mathrm{l}} = \ln \phi^{\mathrm{v}} \tag{7}$$

If we now substitute the formula

$$\ln \phi = \int_{v}^{\infty} \left(\frac{Pv}{RT} - 1 \right) \frac{\mathrm{d}v}{v} + \left(\frac{Pv}{RT} - 1 \right) - \ln \left(\frac{Pv}{RT} \right) \tag{8}$$

into Eq. (7) and simplify, assuming constant pressure conditions, it can be shown that

$$\int_{v^{\mathrm{l}}}^{v^{\mathrm{v}}} \left(\frac{1}{T^{\mathrm{sat}}} - \frac{1}{T} \right) \mathrm{d}v = 0 \tag{9}$$

where T^{sat} is the saturation temperature and v^{l} and v^{v} the saturated liquid and vapor volumes, respectively. The coexistence points are found by applying Eq. (9) to the simulated isobar and solving for the three unknowns T^{sat}, v^{l} and v^{v}.

For these simulations, a system composed of $N = 1372$ LJ atoms was used with a fixed potential cut-off radius of 2.5σ. The isobars were obtained by starting the simulation in the pure liquid phase at an initial enthalpy of H_{l}. The pressure was kept constant at P_{set} using the $N\dot{P}\dot{H}_{\mathrm{c}}$ method, while the enthalpy was increased incrementally with steps of $\Delta H \approx 0.0729$ until a final enthalpy of H_{v} was reached, whereby

Table 4
Isobar pressures, initial and final molar enthalpies, and the computed coexistence temperatures and densities

P_{set}	H_l	H_v	T^{sat}	ρ_l^{sat}	ρ_v^{sat}
0.04511	−3.644	2.915	1.026	0.6914	0.0634
0.05974	−3.279	2.915	1.102	0.6457	0.0825
0.07718	−2.915	2.551	1.176	0.5941	0.1061
0.0973	−2.551	2.551	1.243	0.5348	0.1373
0.1204	−1.093	2.187	1.303	0.4606	0.1795
0.130	−1.093	2.187	1.324	0.4243	0.2104
0.132	−1.093	2.187	1.329	0.4115	0.2146
0.135	−1.093	2.187	1.334	0.3955	0.2249
0.137	−1.093	2.187	1.338	0.3845	0.2372
0.140	−1.093	2.187	1.344	0.3641	0.2459
0.142	−1.093	2.187			
0.144	−1.093	2.187			
0.146	−1.093	2.187			
0.148	−1.093	2.187			
0.150	−1.093	2.187			

the fluid was a pure vapor. Values of the enthalpy and pressure are reported in Table 4. After each step change in the enthalpy, the fluid was allowed to equilibrate for 10,000 timesteps at that state point. The average steady-state density and temperature values at this state point were then calculated from the next 30,000 timesteps, after which another step change in the enthalpy was imposed. Isobars were obtained at different values of P_{set}, both above and below the critical pressure.

The isobars were found to show some fluctuations. To obtain accurate coexistence curves, these fluctuations needed to be filtered out. We employed a running average type filtering of each isobar, and the resulting smooth isobars are plotted in Fig. 10 as dashed lines. The saturation temperatures and volumes were obtained from Eq. (9) using a numerical scheme whereby the integral value at closely spaced trial T^{sat} values was computed. A sign change in the value of the integral denoted the whereabouts of the correct T^{sat}. The computed values of T^{sat}, v^l and v^v are noted in Table 4, and also plotted in Fig. 10 as open squares. For pressures $P_{set} > 0.140$, the isobars do not show any inflection points and are, hence, above the critical point. Alongside, we have also plotted the coexistence data obtained by Lotfi et al. [13] as a dark dashed curve. It is observed that there is a slight mismatch between the two results for the low density leg of the coexistence curve. This could be due to the fact that Lotfi et al. used a larger cut-off of 5.7σ than was used here. It could also be due to inaccuracies with the PHD-MD approach. We observed that the isobars showed greater fluctuations in the two phase region near the vapor phase as the pressure was reduced. Below a pressure of $P = 0.04511$, an instability arose and the system exhibited a tremendous jump in density with a small change in enthalpy. Coexistence points could not be determined below this pressure. This instability is likely due to the fact that, away from the critical point, the energy difference between the metastable vapor and liquid phases becomes so great that the two phase region cannot be adequately simulated with only 1372 atoms. Much larger systems would be required to accurately simulate both phases in this region. For this reason, the PHD-MD results are expected to be least accurate for the vapor phase at low pressure and points out a weakness of the method for computing coexistence curves away from the critical point. Despite these problems, the high-pressure region of the coexistence curve is captured surprisingly well.

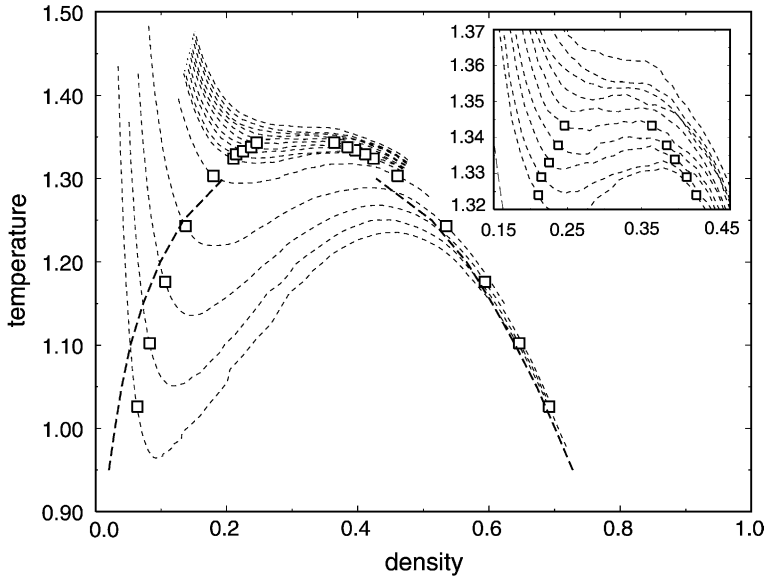

Fig. 10. Dashed lines are simulated isenthalps. Open squares are estimates of coexistence points from the simulation. The coexistence curve computed by Lotfi et al. [13] is shown for comparision. Inset shows detail of simulation results close to the critical point.

Interestingly, the stabilization afforded by the pressure and enthalpy drivers enables the system to be simulated arbitrarily close to the critical point. The inset in Fig. 10 shows a series of isobars near the generally accepted critical point for the LJ fluid. From the inflection point in these isobars, the critical pressure is estimated to lie within the range $0.140 < P_c < 0.142$. This is higher than the generally accepted value, which lies in the range $0.127 \leq P_c \leq 1.31$ [21,23], although other estimates have placed the critical pressure as high as $P_c = 0.147$ [24]. The critical temperature is estimated to be in the range $1.344 < T_c < 1.347$, in fair agreement with a recent estimate of $T_c = 1.31$ [21]. The critical density is estimated as $\rho_c \approx 0.304$, which agrees perfectly with an early estimate [23], but is slightly lower than $\rho_c = 0.316$, the value determined by more recent and extensive calculations [21]. We believe that the estimates of the critical point obtained using the PHD-MD method are encouraging, given that they were based on MD simulations carried out with a single box size (i.e. no finite size scaling methods were used). They appear to be at least as accurate as those obtained using conventional simulation methods, and can, thus, provide a reasonable first estimate of a critical point. It would be interesting to carry out a more extensive study of the method and see if the results can be made even more accurate.

4. Conclusions

Results from a new pressure-enthalpy driven molecular dynamics simulation method were presented. Using the LJ fluid as a test case, it was shown how thermodynamic derivatives such as the Joule–Thomson coefficient and inversion curve can be computed directly from a single molecular dynamics simulation. The approach was also used to simulate a complete vapor-compression refrigeration cycle and a vapor–liquid

coexistence curve, as well as obtain a reasonable estimate of the critical point. The method can be implemented in any standard molecular dynamics package with only small modifications to the equations of motion. It provides a straightforward means for driving a system to any desired thermodynamic state-point using molecular dynamics, and thus represents an attractive means for probing the thermodynamic properties of complex systems.

List of symbols

e	molar internal energy
h	molar enthalpy
H	enthalpy
$\dot{H}$	rate of change of enthalpy
k_Q	entropy driver time constant
K	kinetic energy
m_i	mass of atom i
N	number of molecules in the system
P	pressure
P_c	critical pressure
$\dot{P}$	rate of change of pressure
Q	heat
$\dot{Q}$	rate of heat addition or removal
S	entropy
$\dot{S}$	time derivative of entropy
T	temperature
T^{sat}	saturation temperature
T_c	critical temperature
v_i	velocity of atom i
v^l, v^v	molar volume of liquid, vapor phase
V	system volume

Greek symbols

α	Lagrange multiplier constraining enthalpy
α_S	Lagrange multiplier constraining entropy
μ_{JT}	Joule–Thomson coefficient
ϕ	fugacity coefficient
Φ	potential energy
ρ	density
σ	Lennard–Jones size paramterer

Acknowledgements

Profs. E.A. Müller and F.A. Escobedo are acknowledged for providing their Joule–Thomson inversion curve data. EJM wishes to thank the National Science Foundation for a CAREER award (CTS-9701470). Notre Dame's Center for Applied Mathematics provided partial financial support to GA. We acknowledge

the US Army Research Office (grant DAAG55-98-1-0091) for the computers on which these calculations were performed.

References

[1] L.I. Kioupis, E.J. Maginn, Fluid Phase Equil. 200 (2002) 75–92.
[2] Technology Roadmap for Computational Chemistry, http://209.213.123.21/vision/index/roadmaps/complete.html.
[3] J. Winnick, Chemical Engineering Thermodynamics, Wiley, New York, 1997.
[4] W.G. Kortekaas, C.J. Peters, J. de Swaan Arons, Fluid Phase Equil. 139 (1997) 205–218.
[5] L.I. Kioupis, E.J. Maginn, Chem. Eng. J. 74 (1999) 129–146.
[6] G.J. Martyna, M.E. Tuckerman, D.J. Tobias, M.L. Klein, Mol. Phys. 87 (1996) 1117–1157.
[7] A. Chacín, J.M. Vázquez, E.A. Müller, Fluid Phase Equil. 165 (1999) 147–155.
[8] J.K. Johnson, J.A. Zollweg, K.E. Gubbins, Mol. Phys. 78 (1993) 591–618.
[9] C.M. Colina, E.A. Müller, Mol. Simul. 19 (1997) 237–246.
[10] C.M. Colina, E.A. Müller, Int. J. Thermophys. 20 (1999) 229–235.
[11] D.M. Heyes, C.T. Llaguno, Chem. Phys. 168 (1992) 61–68.
[12] F.A. Escobedo, Z. Chen, Mol. Simul. 26 (2001) 395–416.
[13] A. Lotfi, J. Vrabec, J. Fischer, Mol. Phys. 76 (1992) 1319–1333.
[14] J.A. Izaguirre, D.P. Catarella, J.M. Wozniak, R.D. Skeel, J. Chem. Phys. 114 (2001) 2090–2098.
[15] J.-P. Hansen, L. Verlet, Phys. Rev. 184 (1969) 151–161.
[16] D. Frenkel, B. Smit, Understanding Molecular Simulation, Acadmic Press, San Diego, CA, 1996.
[17] A.Z. Panagiotopoulos, Mol. Phys. 61 (1987) 813–826.
[18] A.Z. Panagiotopoulos, N. Quirke, M. Stapleton, D.J. Tildesley, Mol. Phys. 63 (1988) 527–546.
[19] D.A. Kofke, J. Chem. Phys. 98 (1993) 4149–4162.
[20] A.M. Ferrenberg, R.H. Swendsen, Phys. Rev. Lett. 63 (1988) 1195–1198.
[21] J.J. Potoff, A.Z. Panagiotopoulos, J. Chem. Phys. 109 (1998) 10914–10920.
[22] S.I. Sandler, Chemical and Engineering Thermodynamics, Wiley, New York, 1999.
[23] B. Smit, J. Chem. Phys. 96 (1992) 8639–8640.
[24] J.M. Caillol, J. Chem. Phys. 109 (1998) 4885–4893.